Asociación Argentina
de Mecánica Computacional

Mecánica Computacional Vol XXIX, págs. 3927-3948 (artículo completo)
Eduardo Dvorkin, Marcela Goldschmit, Mario Storti (Eds.)
Buenos Aires, Argentina, 15-18 Noviembre 2010

APPLICATION OF A REYNOLDS-AVERAGED NAVIER-STOKES MODEL TO WAVES IN CHANNELS

Teixeira P.R.F.[a], **Fortes C.J.M.**[b]

[a]*Escola de Engenharia, Universidade Federal do Rio Grande – FURG, Av. Itália, km 8, Campus Carreiros, 96201-900, Rio Grande, RS, Brasil, pauloteixeira@furg.br*

[b]*Departamento de Hidráulica e Ambiente, Laboratório Nacional de Engenharia Civil, Av. do Brasil, 101, 1700-066, Lisboa, Portugal, jfortes@lnec.pt*

Keywords: Free surface, wave propagation, numerical modeling, RANS model, finite element method.

Abstract. Wave-structure interaction and wave propagation on complex topography are very important in Coastal Engineering. They involve phenomena that combine reflection, shoaling, refraction and diffraction that generate harmonics with complex energy transfers. Over the past decades, many numerical models have been developed to deal with these problems. Due to the large horizontal dimensions of the region under study, the numerical solutions of the Navier-Stokes equations have high computational costs to determine the three-dimensional velocity and pressure fields, besides the free surface position. However, when flow separation, vortex or turbulence phenomena are involved, Reynolds-averaged Navier-Stokes models provide more accurate results. The objective of this paper is to apply the FLUINCO model (P. Teixeira and C. Fortes, *Rev. Int. Mét. Num. Cálc. Dis. Ing.*, 25(2):313-336 (2009)) to test cases of wave propagation in channels. FLUINCO employs the two step semi-implicit Taylor-Galerkin fractional method to discretize the Navier-Stokes equations in time and space. The code adopts linear tetrahedral elements and the arbitrary Lagrangian-Eulerian formulation to enable the solution of problems concerning the free surface motion. A smoothing procedure is applied to the mesh velocity distribution to minimize element distortion, considering the velocities of each node belonging to the boundary surface. The first application is the wave propagation in a channel of constant depth. The energy spectrum, pressure and velocity fields produced by the numerical model are compared with linear and nonlinear wave theories. The second case deals with the wave propagation over the trapezoidal submerged breakwaters. Two types of breakwater slopes are studied: the first with upstream and downstream slopes of 1:20 and 1:10, respectively; and the second with both 1:2 slopes. The results of the surface elevation and the energy spectrum at various points in the field as well as the pressure and velocity fields for each breakwater geometry are presented. In the last case, vortices near the upstream slope, that increase nonlinear effects, are found. Finally, the wave propagation over a submerged horizontal cylinder is analyzed and these results are compared with experimental ones. The flow near the cylinder, the free surface and the velocity profiles on several gauges are analyzed.

1 INTRODUCTION

Wave-bottom and wave-structure interactions are important issues in Coastal Engineering. In the last decades, many numerical models have been developed to analyze these cases (Liu, 1995; Wu, 2001) that involve reflection, shoaling, refraction and difraction phenomena. These non-linear effects generate harmonics with high complex energy transfer.

The models based on the Laplace equation assume the potential flow; it is irrotational and the fluid is incompressible. Some examples are models that use the boundary element method (Longuet-Higgins and Cokelet, 1976; Isaacson, 1982; Grilli et al., 2001) and the ones that employ the spectrum methods (Dommermuth and Yue, 1987; Bateman et al., 2001). These types of models are not appropriate to be used in flows that interact with structures involving shearing, separation, vortices and turbulence.

Other models used for simulating wave propagation are named depth-integrated models. Peregrine (1967) developed Boussinesq equations for variable depth, assuming polynomial approaches for the vertical velocity distribution and the vertical integration in resultant equations at a specific depth. The simplified hypotheses that assume weak non-linearity and dispersion restrict the uses in shallow waters. In the last decades, a lot of researches have tried to extend the applicability of these equations to deeper waters and to higher non-linearity including high order terms in the equations. Other phenomena, such as breaking, bottom friction and run-up, are also included in the Boussinesq extended equations. Therefore, nowadays there are several Boussinesq extended equations, for example, those developed by Madsen et al. (1992, 2002), Nwogu (1993), Wei et al. (1995), Gobbi and Kirby (1999), Schäffer and Madsen (1995), Agnon et al. (1999), Kennedy et al. (2001). Recently, this type of model has been improved the depth integration of the continuity and the momentum equations by using the multi-layer concept (multi-layer Boussinesq models) (Lynett and Liu, 2004; Hsiao et al., 2005), i.e., one velocity profile is propose for each layer along the water column. The accuracy of the model depends on the quantity of layers, enabling the employment to deep waters. Although the accuracy of these models has been increasingly improved, the simplified hypotheses related to the velocity profile and their integration along the depth restrict the use of these models on bottoms without significant depth variations.

Many efforts have been made to develop the non-hydrostatic models lately (Casulli and Stelling, 1998; Stansby and Zhou, 1998; Zijlema and Stelling, 2008; Mahadevan et al., 1996; Marshall et al., 1997; Hodges and Street, 1999; Lin and Li, 2002). These are capable of determining the free surface deformations and the velocity field for complex topography cases. They also capture the free surface movements using a function of the horizontal plane and require a lower discretization in vertical direction in comparison to the models that use the classic methods to describe the free surface. Some of these models divide the pressure and the velocity fields in hydrostatic and non-hydrostatic to improve the efficiency of the methods.

Due to the large scale in the horizontal plane, which is common in Coastal Engineering, the numerical solution of the Navier-Stokes equations demands high computational costs to determine the velocity and pressure fields and the free surface position. However, these models provide more realistic results when flow separation, vortices or turbulence occur. Some methods used for describing the water-air interface should be emphasized: the arbitrary lagrangean-eulerian (ALE) formulation (Hodges and Street, 1999; Zhou and Stansby, 1999), the marker and cell method (Harlow and Welch, 1965), the volume of fluid method (VOF) (Lin and Liu, 1998; Hieu et al., 2004) and the level-set method (Iafrati et al., 2001).

The FLUINCO code (Teixeira and Awruch, 2005), employed in this paper, integrates the Navier-Stokes equations using a fractional method to simulate 3D incompressible flows

including problems with free surfaces. It uses the semi-implicit two-step Taylor Galerkin method in order to discretize the Navier-Stokes equations in time and space. It adopts a linear tetrahedral element, which has the advantages of adapting to domains with complex geometries and presenting good computational efficiency. An ALE formulation is used for enabling the solution of problems that involve free surface movements. The element distortions are minimized by smoothing the spatial distribution of the mesh velocity; this procedure uses functions that take into account the velocity influence at each node that belongs to the boundary surfaces.

The applications of FLUINCO to three cases that involve wave propagation are presented in this paper. The first one is the wave propagation in a channel of constant depth. The energy spectrum, pressure and velocity fields produced by the numerical model are compared with linear and nonlinear wave theories. The second case is related to the wave propagation over the trapezoidal submerged breakwaters. Two types of breakwater slopes are studied: the first with upstream and downstream slopes of 1:20 and 1:10, respectively; and the second with both 1:2 slopes. The results of the surface elevation and the energy spectrum at various points in the field as well as the pressure and velocity fields for each breakwater geometry are presented. Finally, the wave propagation over a submerged horizontal cylinder is analyzed and these results are compared with experimental ones. The flow near the cylinder, the free surface and the velocity profiles on several gauges are analyzed.

Chapter 2 describes the FLUINCO model. Chapter 3 presents the study case results and discussions. Finally, conclusions are in Chapter 4.

2 FLUINCO MODEL

2.1 Governing equations for fluid flows

Mass conservation for slightly compressible fluids, assuming constant entropy, may be expressed by the following equation:

$$\frac{\partial \rho}{\partial t} = \frac{1}{c^2}\frac{\partial p}{\partial t} = -\frac{\partial U_i}{\partial x_i} \quad (i=1,2,3), \tag{1}$$

where ρ is the specific mass, c is the sound speed, $U_i = \rho \, \mathrm{v}_i$ and v_i are the fluid velocity components.

Equations expressing both momentum and energy conservation in ALE description complete the governing equations of the fluid flow problem:

$$\frac{\partial (U_i)}{\partial t} + \frac{\partial (f_{ij})}{\partial x_j} + \frac{\partial p}{\partial x_i} - \frac{\partial \tau_{ij}}{\partial x_j} - \rho g_i = \mathrm{w}_j \frac{\partial (U_i)}{\partial x_j} \quad (i,j=1,2,3), \tag{2}$$

$$\frac{\partial (\rho e)}{\partial t} + \frac{\partial (\rho e \, \mathrm{v}_i)}{\partial x_i} - \frac{\partial}{\partial x_j}\left(k \frac{\partial T}{\partial x_j} \right) = \mathrm{w}_j \frac{\partial (\rho e)}{\partial x_j} \quad (i,j=1,2,3), \tag{3}$$

where w_i are the mesh velocity components, T is the temperature, e is the internal specific energy, k is the thermal conductivity and g_i are the gravity acceleration components. $\tau_{ij} = \mu\left(\frac{\partial \mathrm{v}_i}{\partial x_j} + \frac{\partial \mathrm{v}_j}{\partial x_i} \right) + \lambda \frac{\partial \mathrm{v}_k}{\partial x_k} \delta_{ij}$ are the components of the deviatory tensor, μ and λ are the shear and volumetric viscosity coefficients, respectively, δ_{ij} is the Kroenecker delta and $f_{ij} = \mathrm{v}_j (\rho \, \mathrm{v}_i) = \mathrm{v}_j U_i$. Initial and boundary conditions must be added to Eq. (1), (2) and (3) in

order to define the problem uniquely. In incompressible flows, the energy equation, Eq. (3), can be solved independently, after the field of velocities is computed.

2.2 Time and space discretizations

The variables U_i are discretized in time domain using a Taylor series expansion. In the first step, corresponding to the time interval [t_n, $t_{n+1/2}$], U_i are given by the following expression (Teixeira and Awruch, 2000):

$$U_i^{n+1/2} = U_i^n + \frac{\Delta t}{2}\frac{\partial U_i^n}{\partial t} = U_i^n - \frac{\Delta t}{2}\left(\frac{\partial f_{ij}^n}{\partial x_j} - \frac{\partial \tau_{ij}^n}{\partial x_j} + \frac{\partial p^n}{\partial x_i} + \frac{1}{2}\frac{\partial \Delta p}{\partial x_i} - w_j^n \frac{\partial U_i^n}{\partial x_i}\right) \quad (i,j=1,2,3)\,, \tag{4}$$

where $p^{n+1/2} = p^n + 1/2\,\Delta p$, with $\Delta p = p^{n+1} - p^n$. Using

$$\tilde{U}_i^{n+1/2} = U_i^n - \frac{\Delta t}{2}\left(\frac{\partial f_{ij}^n}{\partial x_j} - \frac{\partial \tau_{ij}^n}{\partial x_j} + \frac{\partial p^n}{\partial x_i} - w_j^n \frac{\partial U_i^n}{\partial x_i}\right) \quad (i,j=1,2,3)\,. \tag{5}$$

Eq. (4) is given by the following expression:

$$U_i^{n+1/2} = \tilde{U}_i^{n+1/2} - \frac{\Delta t}{4}\frac{\partial \Delta p}{\partial x_i} \quad (i=1,2,3)\,. \tag{6}$$

By discretizing Eq. (1) in time and applying Eq. (6), the result is:

$$\Delta\rho = \frac{1}{c^2}\Delta p = -\Delta t \frac{\partial U_i^{n+1/2}}{\partial x_i} = -\Delta t\left[\frac{\partial \tilde{U}_i^{n+1/2}}{\partial x_i} - \frac{\Delta t}{4}\frac{\partial}{\partial x_i}\frac{\partial \Delta p}{\partial x_i}\right] \quad (i = 1,2,3)\,. \tag{7}$$

The second step is given by the following expression:

$$U_i^{n+1} = U_i^n + \Delta t \frac{\partial U_i^{n+1/2}}{\partial t} = U_i^n - \Delta t\left(\frac{\partial f_{ij}^{n+1/2}}{\partial x_j} - \frac{\partial \tau_{ij}^{n+1/2}}{\partial x_j} + \frac{\partial p^{n+1/2}}{\partial x_i} - w_j^{n+1/2}\frac{\partial U_i^{n+1/2}}{\partial x_i}\right) \quad (i,j=1,2,3). \tag{8}$$

After space discretization, the flow is analyzed by the following algorithm: (a) determine $\tilde{U}_i^{n+1/2}$ with Eq. (5); (b) determine Δp with Eq. (7) and calculate $p^{n+1} = p^n + \Delta p$; (c) determine $U_i^{n+1/2}$ with Eq. (6); and (d) determine U_i^{n+1} with Eq. (8).

The classical Galerkin weighted residual method is applied to the space discretization. In the variables at $t+\Delta t/2$ instant, a constant shape function PE is used, and in the variables at t and $t+\Delta t$, a linear shape function N is employed. By applying this procedure to Eq. (5), (7), (6) and (8), the following expressions in the matrix form are obtained (Teixeira and Awruch, 2000):

$$\Omega_E^{n+1/2}\,\tilde{\overline{\mathbf{U}}}_i^{n+1/2} = \mathbf{C}\;\overline{\mathbf{U}}_i^n - \frac{\Delta t}{2}\left[\mathbf{L}_j\left(\overline{\mathbf{f}}_{ij}^n - \overline{\boldsymbol{\tau}}_{ij}^n\right) + \mathbf{L}_i\,\overline{\mathbf{p}}^n - \mathbf{T}\;\overline{\mathbf{U}}_i^n - \Omega_E^{n+1/2}\,\overline{\rho g}_i\right] \tag{9}$$

$$\left(\tilde{\mathbf{M}} + \frac{\Delta t^2}{4}\mathbf{H}\right)\Delta\overline{\mathbf{p}} = \Delta t\left(\mathbf{L}_i^T\,\tilde{\overline{\mathbf{U}}}_i^{n+1/2} + \mathbf{f}_a\right) \tag{10}$$

$$\overline{\mathbf{U}}_i^{n+1/2} = \tilde{\overline{\mathbf{U}}}_i^{n+1/2} - \frac{\Delta t}{4\,\Omega_E}\mathbf{L}_i\,\Delta\overline{\mathbf{p}} \tag{11}$$

$$\mathbf{M}^{n+1}\,\overline{\mathbf{U}}_i^{n+1} = \mathbf{M}^n\,\overline{\mathbf{U}}_i^n + \Delta t\left[\mathbf{L}_j^T\left(\overline{\mathbf{f}}_{ij}^{n+1/2} - \overline{\mathbf{w}}_j^{n+1/2}\,\overline{\mathbf{U}}_i^{n+1/2}\right) - \mathbf{Q}_j\,\overline{\boldsymbol{\tau}}_{ij}^n + \mathbf{Q}_i\left(\overline{\mathbf{p}}^n + \Delta\overline{\mathbf{p}}/2\right) + \mathbf{S}_{bi} - \mathbf{C}^T\,\overline{\mathbf{g}}_i\right] \tag{12}$$

where variables with upper bars at n and n+1 instants indicate nodal values, while those at n+1/2 instant represent constant values in the element. The matrices and vectors from Eq. (9) to (12) are volume and surface integrals that were obtained by applying the classical Galerkin method. They are expressed by (Teixeira and Awruch, 2000):

$$\begin{aligned}
&\Omega_E^{n+1/2} = \int_{\Omega^{n+1/2}} \mathbf{P}_E^T \mathbf{P}_E \; d\Omega \qquad \mathbf{C} = \int_{\Omega^n} \mathbf{P}_E^T \mathbf{N} \; d\Omega \qquad \mathbf{L}_i = \int_{\Omega^n} \mathbf{P}_E^T \frac{\partial \mathbf{N}}{\partial x_i} \; d\Omega \\
&\mathbf{T} = \int_{\Omega^n} \mathbf{P}_E^T \mathbf{N} \overline{\mathbf{w}}_i^n \frac{\partial \mathbf{N}}{\partial x_i} \; d\Omega \qquad \tilde{\mathbf{M}} = \int_{\Omega^{n+1/2}} \mathbf{N}^T \left(\frac{1}{c^2} \right) \mathbf{N} \; d\Omega \qquad \mathbf{H} = \int_{\Omega^{n+1/2}} \frac{\partial \mathbf{N}^T}{\partial x_i} \frac{\partial \mathbf{N}}{\partial x_i} \; d\Omega \\
&\mathbf{f}_a - \int_{\Gamma^{n+1/2}} \mathbf{N}^T \mathbf{P}_E \mathbf{n}_i \tilde{\overline{\mathbf{U}}}_i^{n+1/2} d\Gamma \qquad \mathbf{M}^n = \int_{\Omega^n} \mathbf{N}^T \mathbf{N} \; d\Omega \qquad \mathbf{Q}_i = \int_{\Omega^n} \frac{\partial \mathbf{N}^T}{\partial x_i} \mathbf{N} \; d\Omega \\
&\mathbf{S}_{bi} = -\int_{\Gamma^{n+1/2}} \mathbf{N}^T \mathbf{P}_E \mathbf{n}_j d\Gamma \left(\overline{\mathbf{f}}_{ij}^{n+1/2} - \overline{\mathbf{w}}_j^{n+1/2} \overline{\mathbf{U}}_i^{n+1/2} \right)
\end{aligned} \tag{13}$$

Equation (10) is solved using the conjugated gradient method with diagonal pre-conditioning. In Eq. (12), the consistent mass matrix is substituted by the lumped mass matrix, and then this equation is solved iteratively.

2.3 Kinematic free surface boundary condition (KFSBC)

The free surface is the interface between two fluids, water and air, where atmospheric pressure is considered constant (generally the reference value is null). In this interface, the KFSBC is imposed. By using the ALE formulation, it is expressed as (Ramaswamy and Kawahara, 1987):

$$\frac{\partial \eta}{\partial t} + \left({}^{(s)}\mathrm{v}_i - {}^{(s)}\mathrm{w}_i \right) \frac{\partial \eta}{\partial x_i} = 0 \quad (i=1,2,3) \,, \tag{14}$$

where η is the free surface elevation, ${}^{(s)}\mathrm{v}_i$ and ${}^{(s)}\mathrm{w}_i$ are the fluid and mesh velocity components in the free surface, respectively. The eulerian formulation is used in the x and y directions (horizontal plane) while the ALE formulation is employed in the z or vertical direction.

The time discretization of KFSBC is carried out in the same way as the one for the momentum equations as presented before. After applying expansion in Taylor series, the expressions for η at n+1/2 (first step) and n+1 (second step) instants are obtained:

$$\begin{aligned}
\eta^{n+1/2} &= \eta^n + \frac{\Delta t}{2} \left({}^{(s)}\mathrm{v}_3 - {}^{(s)}\mathrm{v}_1 \frac{\partial \eta}{\partial x_1} - {}^{(s)}\mathrm{v}_2 \frac{\partial \eta}{\partial x_2} \right)^n \\
\eta^{n+1} &= \eta^n + \Delta t \left({}^{(s)}\mathrm{v}_3 - {}^{(s)}\mathrm{v}_1 \frac{\partial \eta}{\partial x_1} - {}^{(s)}\mathrm{v}_2 \frac{\partial \eta}{\partial x_2} \right)^{n+1/2}
\end{aligned} \tag{15}$$

The triangular elements coincide with the face of the tetrahedral elements on the free surface. By adopting a linear triangular element and applying the Galerkin method to Eq. (15), these equations can be written as:

$$\int_{A^{n+1/2}} \mathbf{N}_s^T \mathbf{N}_s \, dA \;\; \overline{\boldsymbol{\eta}}^{n+1/2} = \int_{A^n} \mathbf{N}_s^T \mathbf{N}_s \, dA \;\; \overline{\boldsymbol{\eta}}^{n} + \frac{\Delta t}{2}\left(\int_{A^n} \mathbf{N}_s^T \mathbf{N}_s \, dA \; \overline{\mathbf{v}}_3^{n} - \int_{A^n} \mathbf{N}_s^T \mathbf{N}_s \, dA \left({}^{(s)}\overline{\mathrm{v}}_i \frac{\partial \eta}{\partial x_i} \right)^n \right)$$

$$\int_{A^{n+1}} \mathbf{N}_s^T \mathbf{N}_s \, dA \;\; \overline{\boldsymbol{\eta}}^{n+1} = \int_{A^n} \mathbf{N}_s^T \mathbf{N}_s \, dA \;\; \overline{\boldsymbol{\eta}}^{n} + \Delta t\left(\int_{A^{n+1/2}} \mathbf{N}_s^T \mathbf{N}_s \, dA \; \overline{\mathbf{v}}_3^{n+1/2} - \int_{A^{n+1/2}} \mathbf{N}_s^T \mathbf{N}_s \, dA \left({}^{(s)}\overline{\mathrm{v}}_i \frac{\partial \eta}{\partial x_i} \right)^{n+1/2} \right) \tag{16}$$

where i =1,2; A is the triangular element area, N_s is the linear shape function, $\overline{\boldsymbol{\eta}}^{n}$, $\overline{\boldsymbol{\eta}}^{n+1/2}$ and $\overline{\boldsymbol{\eta}}^{n+1}$ are nodal values of elevations at $t, t+\Delta t/2$ and $t+\Delta t$ instants, respectively. Equations (16) are solved in an iterative form in the same way as in the momentum equations.

2.4 Mesh movement

The mesh velocity vertical component w_3 is computed to diminish element distortions, keeping prescribed velocities on moving (free surface) and stationary (bottom) boundary surfaces. The mesh movement algorithm adopted in this paper uses a smoothing procedure for the velocities based on these boundary surfaces. The updating of the mesh velocity at point i of the finite element domain is based on the mesh velocity of the points j that belong to the boundary surfaces, and is expressed in the following way (Teixeira and Awruch, 2005):

$$w_3^i = \frac{\sum_{j=1}^{ns} a_{ij} \, w_3^j}{\sum_{j=1}^{ns} a_{ij}} \tag{17}$$

where ns is the total number of points belonging to the boundary surfaces and a_{ij} are the influence coefficients between the point i inside the domain and the point j on the boundary surface given by the following expression:

$$a_{ij} = \frac{1}{d_{ij}^4} \tag{18}$$

with d_{ij} being the distance between points i and j. In other words, a_{ij} represents the weight that every point j on the boundary surface has on the value of the mesh velocity at points i inside the domain. When d_{ij} is low, a_{ij} has a high value, favouring the influence of points i, located closer to the boundary surface containing point j.

3 NUMERICAL SIMULATIONS

3.1 Monochromatic wave in a channel

In this case study, a 0.02 high monochromatic wave with a period equal to T=2.02s propagates in a 0.4m deep and 23m long channel. The wavelength is L=3.73m and the wave celerity is C=1.85m/s, according to the linear theory. The end zone of the channel (12m long) is used to damp the reflection effects. These characteristics are the same ones used to the breakwater cases, enabling the observation of the code behavior without the breakwater.

In this case, kh=0.674, where k=2π/L is the wave number and h is the depth. This parameter shows that the wave propagates in intermediate waters ($0.314 < \mathrm{kh} < 3.142$). The parameter H/h=0.05 is lower than breaking theoretical limit; approximately 0.8 (Dean and Dalrymple, 2002). The parameters $\mathrm{h/T^2}=0.098\mathrm{m/s^2}$ and $\mathrm{H/T^2}=0.0049\mathrm{m/s^2}$ show that both linear (Airy) and second order Stokes theories may represent the wave behavior adequately (Chakrabarti, 1994). The Ursell number $U_r = (\mathrm{H/h})^3 / (\mathrm{H/L})^2 = 4.35$ indicates that the non-

linear effects can influence the wave propagation. Since the wave propagation can be represented by linear and second order Stokes theories, the results presented in this paper are compared with those obtained by both theories.

After preliminary tests, we have concluded that the coarser element finite mesh which provided satisfactory results has 20 layers and horizontal size equal to Δx=0.08m (47 points per wavelength), containing 44000 elements and 18522 nodes. There is only one element layer in transversal direction, because of the 2D behavior of the flow.

The velocity components and the elevation of the wave are imposed on one side of the channel. The radiation condition, according to Flather (1976), is imposed on the other side of the channel. The non-slip and kinematic boundary conditions are imposed on the bottom and free surface, respectively. The time step is equal to Δt=0.001s.

The calculated wavelength and celerity (considering numerical results between t=18.0s and 20.0s) were 3.71m to 3.75m and 1.85m/s to 1.87m/s, respectively. These values are closed to those obtained by the linear theory (L=3.73m and C=1.85m/s).

Figure 1 shows the free surface elevation at instant 30s. We can observe the regularity of the wave along the channel.

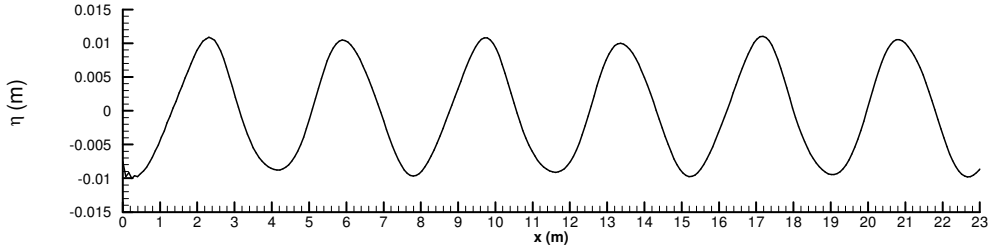

Figure 1: Free surface elevation along the channel at t=30s.

The following results are obtained at x=10.5m position. In Fig. 2, free surface elevations along the time are compared with the ones from linear and non-linear (second order Stokes) theories. We can notice that these results are similar, having obtained more agreement with the non-linear theory.

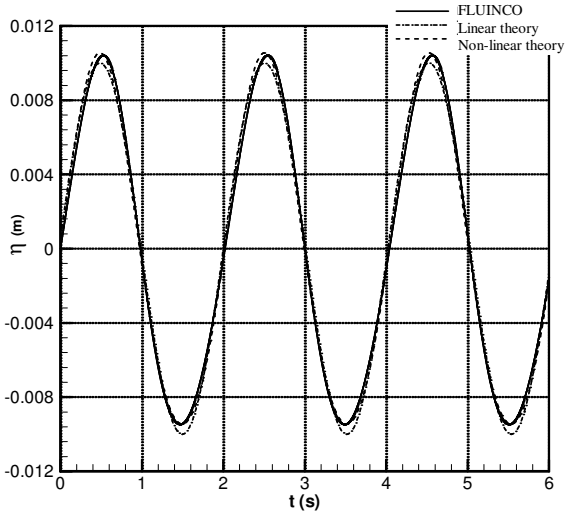

Figure 2: Channel case. Free surface elevation along the time on gauge at x=10.5m.

The velocity component profiles at upward zero-crossing (t=0.0s), crest (t=0.505s), downward zero-crossing (t=1.01s), trough (t=1.515s) and another upward zero-crossing

(t=2.02s) are shown in Figure 3 and are compared with those obtained by the non-linear theory. In general, the vertical profiles present good regularity along the depth, showing that the number of the vertical layers is adequate. The agreement among non-linear theoretical profiles and numerical ones is satisfactory. We can observe the little disturbance of the horizontal velocity component close to the bottom, due to the non-slip boundary condition and the little discretization used in the region to represent the boundary layer adequately. The maximum and the minimum values of the horizontal component are higher than the theoretical ones, but the difference between them is similar to the one predicted by the theory. The vertical component presents some phase differences and the minimum value is lower than the theoretical one.

The horizontal and vertical velocity components along the time on the free surface and at 0.1m (h/4), 0.2m (h/2) and 0.3m (3h/4) depths are presented in Figure 4. We can observe that the closer to the bottom, the more the velocity magnitude components decrease, but they keep approximately the same shape along the time.

Figure 5 shows the numerical velocity components at the average depth (z = -0.2) along the time and their results obtained by non-linear theory. We may notice that the numerical results are similar to non-linear theoretical ones, but some deformations are found even though they do not exist in the theory. The minimum velocity values have a little increment comparing with the theoretical ones. The comments about Figure 3 are confirmed by analyzing Figure 5.

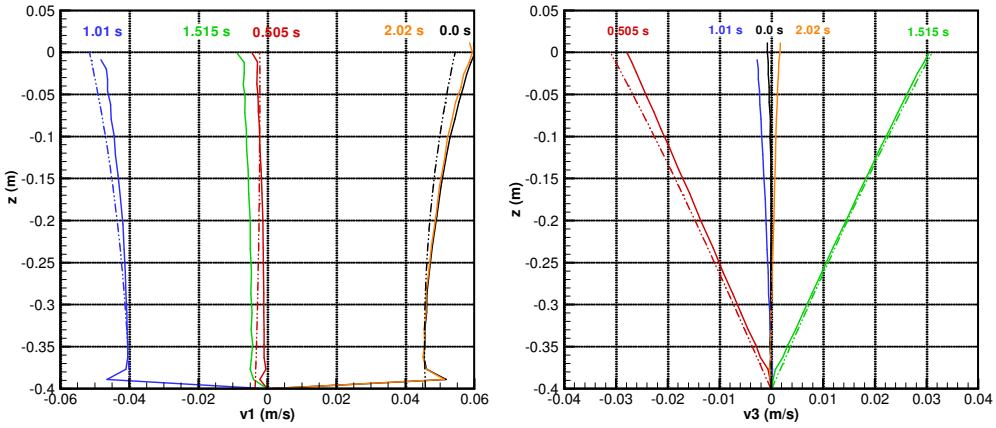

Figure 3: Channel case. Velocity component profiles along the wave cycle. FLUINCO – continuous line, non-linear theory – dashdot line.

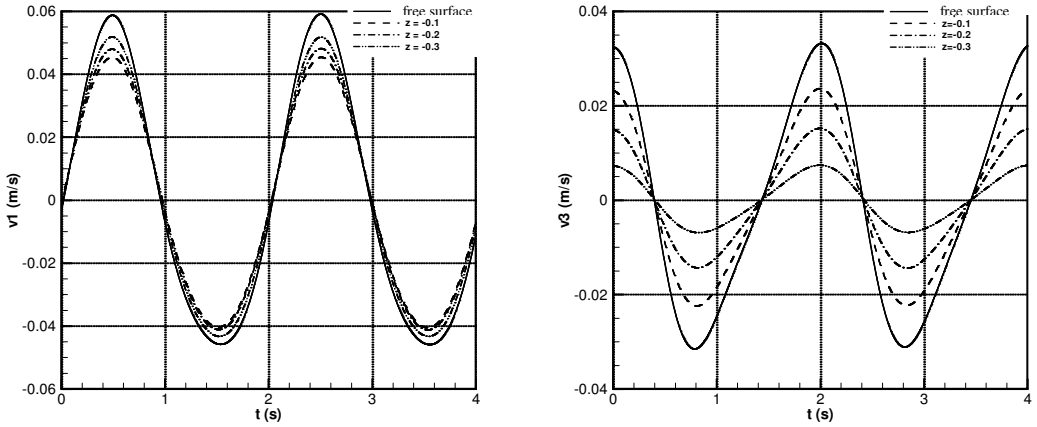

Figure 4: Channel case. Horizontal and vertical velocity components along the time on free surface at 0.1m, 0.2m

and 0.3m depths.

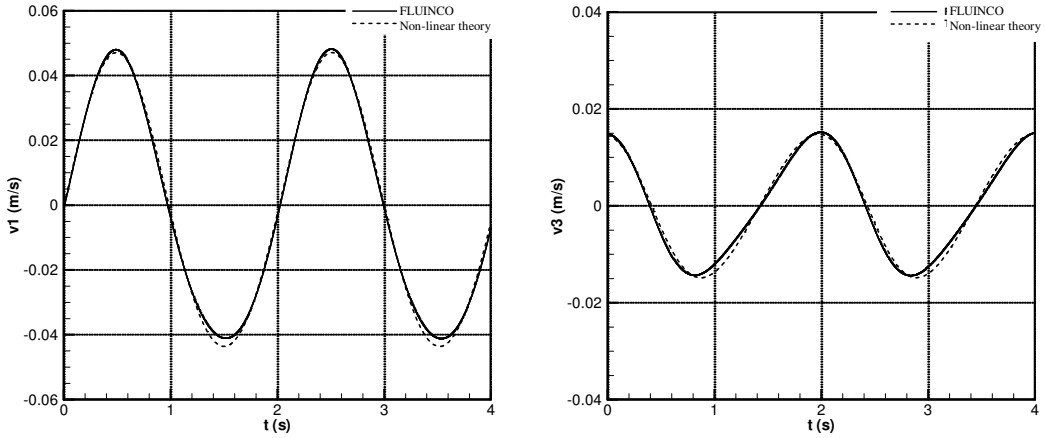

Figure 5: Channel case. Comparison among velocity components at the average depth along the time with non-linear theoretical ones.

The pressures along the time at 0.1m (h/4), 0.2m (h/2), 0.3m (3h/4) and 0.4m (h) depths are shown in Figure 6. The results are compared with those predicted by the linear theory. Although the numerical results are very similar to theoretical ones, the former have the tendency to overestimate the maximum and the minimum values.

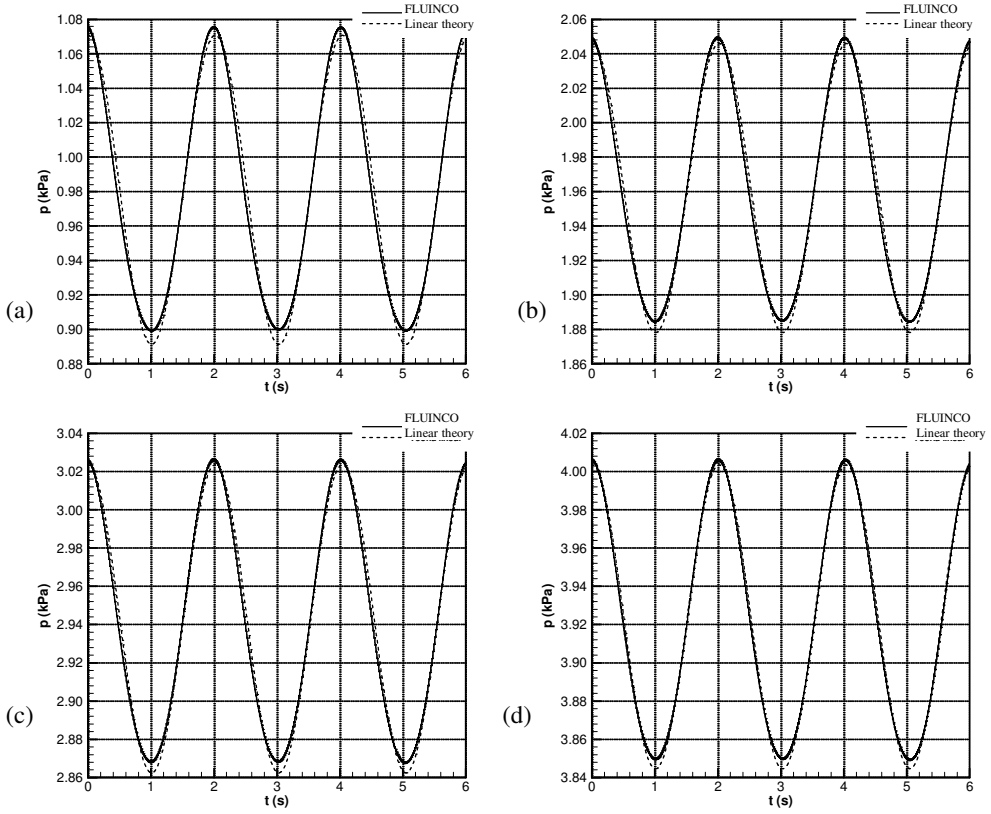

Figure 6: Channel case. Pressure along the time at (a) 0.1m, (b) 0.2m, (c) 0.3m and (d) 0.4m depths.

The frequency spectrum obtained by numerical simulation is presented in Figure 7. We may notice that the wave energy is essentially concentrated on fundamental frequency (f=0.495Hz) and second harmonic frequency (f=0.990Hz), showing the presence of non-linear effects. The amplitudes for fundamental and second harmonic frequencies are 0.0072m and 0.0012m, while the amplitudes predicted by second order Stokes theory are 0.01m and 0.00055m, respectively. We may observe that the fundamental frequency is underestimated whereas the second harmonic is overestimated; it indicates that the numerical results are more dispersive than the theoretical ones.

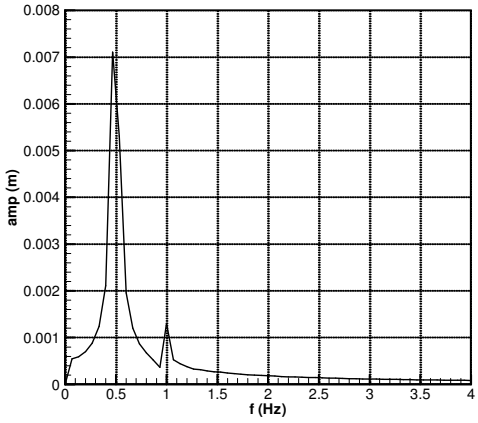

Figure 7: Channel case. Frequency spectrum.

The results presented in this case have shown that the conditions assumed to apply the FLUINCO code to determine free surface elevation, pressure and velocity fields, and frequency spectrum are adequate.

3.2 Breakwater cases

Wave harmonic generation (Johnson et al., 1951; Jolas, 1960) and vortex formation (Huang and Dong, 1999) can occur in wave propagation over submerged breakwaters; it depends on the breakwater geometry. When waves propagate over a submerged obstacle in shallow waters, a quantity of wave energy is transferred from fundamental wave to their harmonics, contributing to increase the non-linearity. Harmonic generation due to wave propagation over obstacles, such as natural reefs, was studied theoretically (Peregrine, 1967), experimentally (Beji and Battjes, 1993; Dingemans, 1994; Ohyama et al., 1995) and numerically (Zhou and Stansby, 1999; Lin and Li, 2002; Casulli, 1999; Yuan and Wu, 2004; Stelling and Zijlema, 2005; Ohyama et al., 1995; Beji and Battjes, 1994; Shen et al., 2004). In some cases, the correct flow simulation is only carried out if viscosity effects are considered (Ting and Kim, 1994; Huang and Dong, 2001). It is important to emphasize that vortices around the breakwater can cause erosion.

Two different configurations of the trapezoidal breakwaters, with different level of non-linearity, are used to test the behavior of the numerical models. In the first case, the downstream and upstream slopes are 1:20 and 1:10, respectively (Dingemans, 1994). In the second one, both slopes are 1:2 (Ohyama et al., 1995), where the non-linear effects are more significant.

3.2.1 Breakwater with slopes 1:20 and 1:10

Figure 8 shows the channel and the submerged breakwater geometries, and the position of the gauges. The channel is 23m in length, 0.4m and 0.1m are the maximum and the minimum depths, respectively. In the channel entrance, a monochromatic wave is generated with period of 2.02s and amplitude of 0.01m.

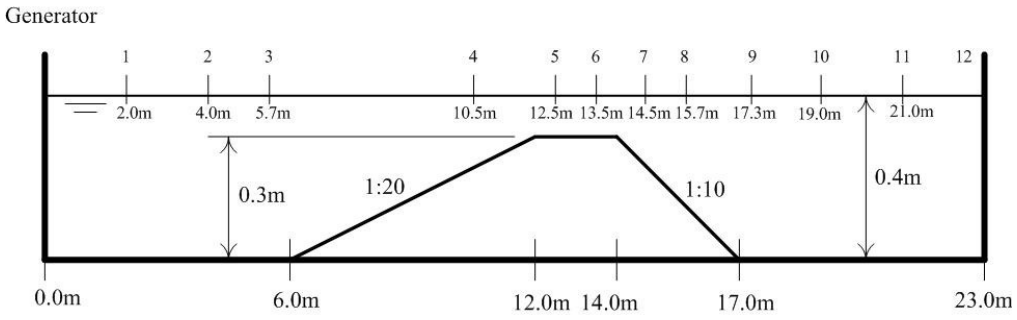

Figure 8: Channel geometry for the 1:20 and 1:10 breakwater

Table 1 presents some parameters for this case study. H/h, even on the platform, has small values in comparison with breaking limit of approximately 0.8 (Dean and Dalrymple, 2002). The case involves intermediate water for the channel ($0.314 < kh < 3.142$) and shallow water for the platform ($kh < 0.314$). Ursell numbers show that the non-linear effects on the platform are more intensive.

	H/h	**kh**	**Ur**
Channel (h = 0.4m)	0.050	0.674	5.0
Platform (h = 0.1m)	0.259	0.318	103.6

Table 1: Wave parameters for the 1:20 and 1:10 breakwater.

Table 2 presents periods, frequencies and wavelengths concerning the fundamental frequency and the harmonic components that occur along the wave propagation. The wavelength was estimated according to the dispersion equation of the linear theory. These values are references to determine discretizations in time and space to be used in the modeling.

	Fundamental	**2nd harmonic**	**3rd harmonic**	**4th harmonic**
Period (s)	2.02	1.01	0.67	0.50
Frequency (Hz)	0.50	1.00	1.50	2.00
Wavelength (m)	3.73	1.46	0.70	0.39

Table 2: Period, frequency and wavelength concerning the fundamental frequency, and 2nd, 3rd and 4th harmonics for the 1:20 and 1:10 breakwater

FLUINCO used a mesh with 88700 elements and 37296 nodes. Twenty layers of elements were used in vertical direction, where small elements are located near the bottom and the free surface. Along the channel, the element sizes vary from $\Delta x = 0.08$m in the boundary to $\Delta x = 0.025$m around the platform. In the transversal direction, only one layer of elements is used, because the behavior of the flow is bi-dimensional. In the entrance of the domain, the wave generation condition is imposed while at the end the radiation condition is imposed. The velocity components are null on the bottom and the KBC is imposed in the free surface. The

velocity component perpendicular to the surface is null for lateral walls (symmetry condition). As an initial condition, the velocity field is null and the pressure one is hydrostatic. The time step is 0.003s, a fact that satisfies the Courant stability condition.

Figure 9 shows the free surface elevations on gauge 3, located downstream the breakwater (x=5.7m); on gauge 6, on the platform (x=13.5m); on gauge 8, in the middle of the upstream slope (x=15.7m); and on gauge 11, on the upstream and far from the breakwater (x=23m). Results obtained by FLUINCO are compared with those obtained by COULWAVE (Lynett and Liu, 2004) and BOUSSiiW (Pinheiro, 2007), both Boussinesq models, and experimental ones presented by Dingemans (1994).

In general, there is good agreement between numerical results and experimental ones on gauges 3 and 6. On gauge 6, FLUINCO presents slightly smooth surface deformation, while BOUSSiiW differs a little more in oscillations with higher frequencies. On gauges 8 and 11, corresponding to downstream, the nonlinear effects are more significant. The deformations on gauge 8 are well represented by FLUINCO and COULWAVE. Although the FLUINCO results get closer to the experimental ones in some regions, there are difficulties in representing the deformations related to higher harmonics, possibly due to the lack of an appropriate discretization to capture the nonlinear phenomena. FLUINCO has a better behavior in relation to the others on gauge 11.

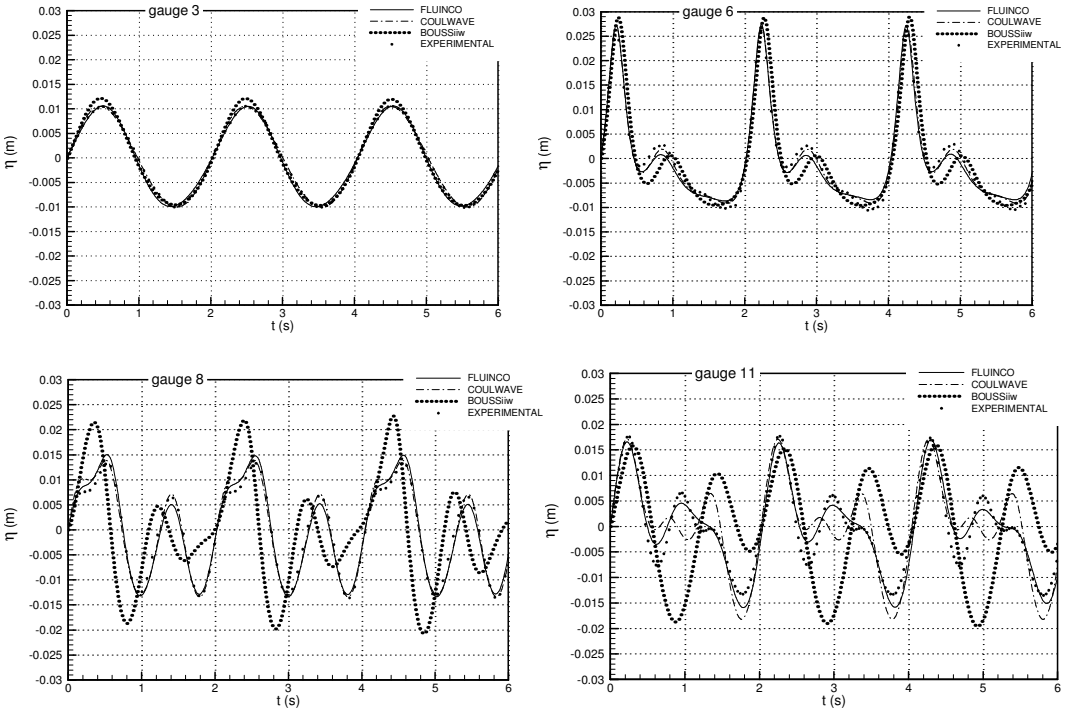

Figure 9: Free surface elevation of the 1:20 and 1:10 breakwater

Figure 10 shows the frequency spectra obtained by models (FLUINCO, COULWAVE and BOUSSiiW) in the gauges and a comparison with the experimental results. The differences found in the free surface elevation are confirmed in Figure 3, which shows differences in the intensity of harmonic components, mainly on gauges located at the end of the channel. The numerical models adequately simulate the position of the peaks of the fundamental frequency and the harmonic components throughout the domain. However, there are some differences in

the amplitude of these peaks, especially on gauges 8 and 11.

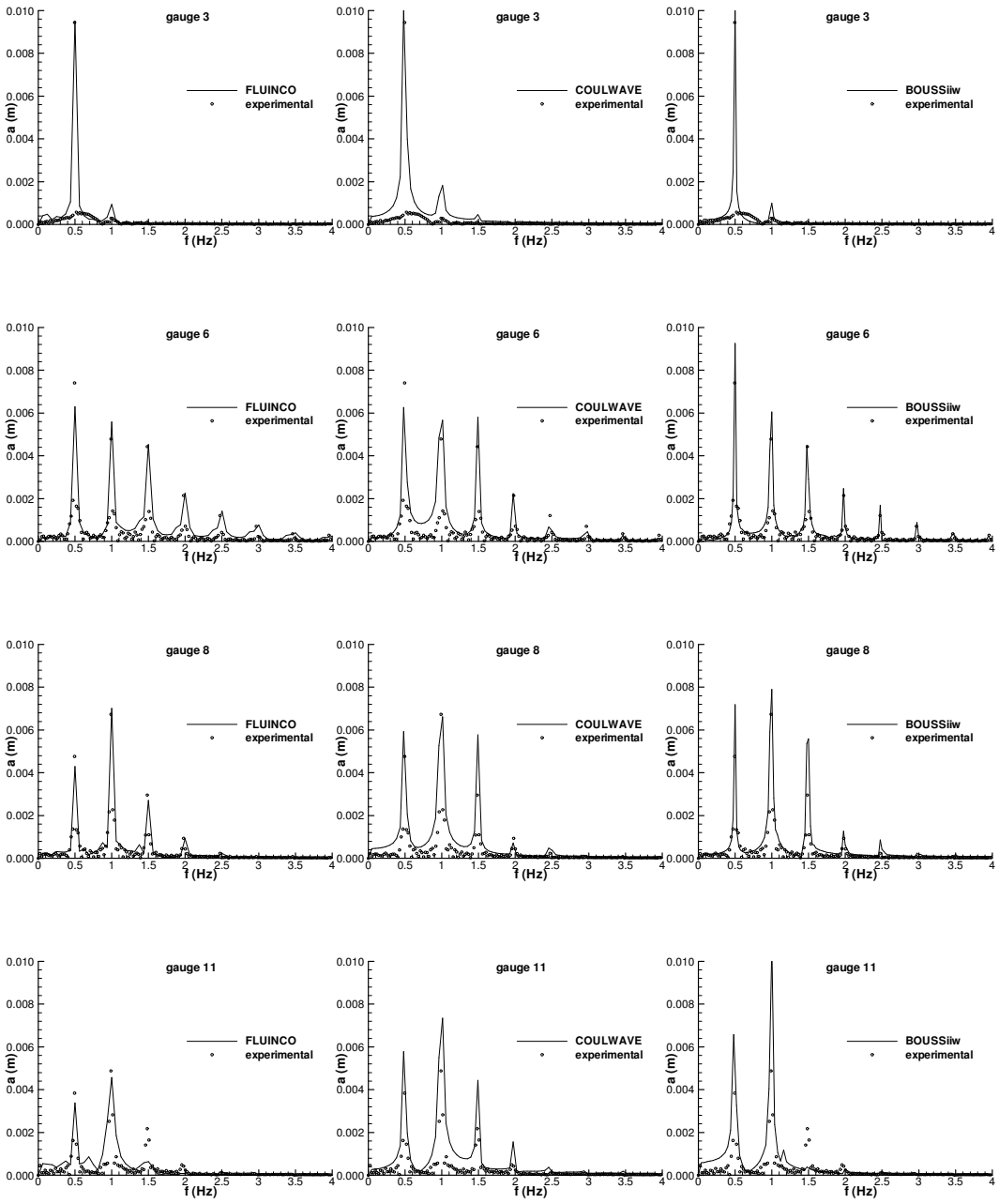

Figure 10: Numerical and experimental frequency spectrum in the gauges of the breakwater 1:20 and 1:10

Figure 11 presents the streamlines around the upstream slope of the breakwater in eleven instants completing one wave period obtained by FLUINCO. We can observe that the flow separation and the vortex do not exist at all instants, due to the mild inclination of the upstream slope.

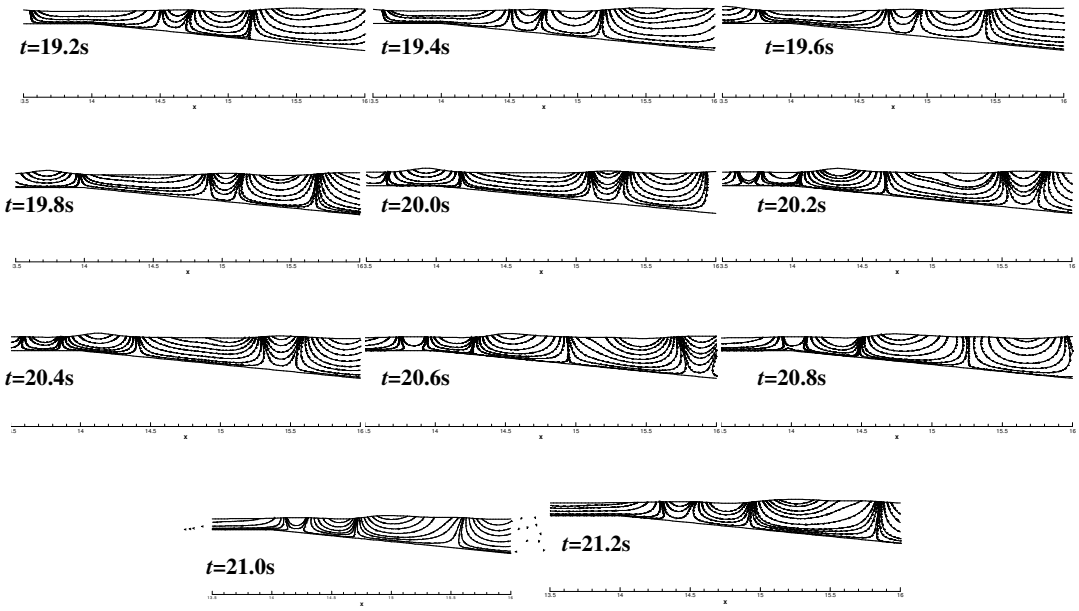

Figure 11: Streamlines of the 1:20 and 1:10 breakwater

3.2.2 Breakwater with slopes 1:2

In this case, the length of the channel is 35m and the maximum and the minimum depths are 0.5m and 0.15m, respectively (see Fig. 12). In the entrance of the channel, a monochromatic wave is generated with a period of 2.68s, related to a wavelength of 5.66m in the channel, and an amplitude of 0.025m. This problem is case 6 studied by Ohyama et al. (1995) who analyzed six different types of waves experimentally. Table 3 shows some parameters that characterize the problem, calculated according to the linear theory. The Ursell number on the platform is 210, indicating the strong non-linearity in this region. Parameter H/h shows that breaking does not even occur on the platform.

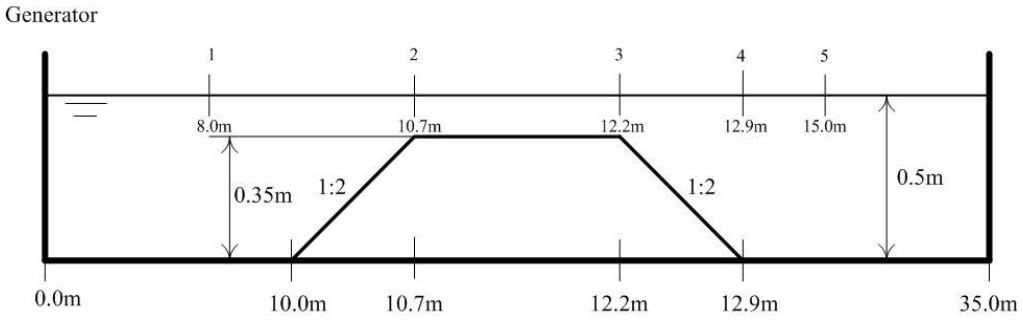

Figure 12: Geometry of the channel for the 1:2 breakwater

	H/h	kh	Ur
Channel (h = 0.5m)	0.100	0.555	14.1
Platform (h = 0.15m)	0.355	0.294	210.0

Table 3: Wave parameters for the 1:2 breakwater

Table 4 shows periods, frequencies and wavelengths concerning the fundamental frequency and the harmonic components that occur along the wave propagation.

A mesh with 120200 elements and 50526 nodes was used for FLUINCO in this simulation. The element sizes along the channel vary between Δx=0.08m at the ends and Δx=0.01m on the platform. The boundary and the initial conditions are similar to the ones in the previous case, and 0.002s was the time step.

	Fundamental	**2nd harmonic**	**3rd harmonic**	**4th harmonic**
Period (s)	2.68	1.34	0.89	0.67
Frequency (Hz)	0.373	0.746	1.124	1.493
Wavelength (m)	5.66	2.42	1.22	0.70

Table 4: Period, frequency and wavelength related to the fundamental frequency, and 2nd, 3rd, and 4th harmonics for the 1:2 breakwaters

Figure 13 shows the free surface elevations on gauges 3 and 5 (gauge positions are indicated in Fig. 5). Numerical results (FLUINCO, COULWAVE and BOUSSiiW) are compared with the experimental ones presented by Ohyama et al. (1995). The FLUINCO and the COULWAVE models represent the surface deformation recorded on gauge 3 well, while BOUSSiiW presents some numerical oscillations of higher frequency. The deformations of gauge 5 indicate that the nonlinearity increases. In this case, FLUINCO captures the variation of the surface elevation more accurately.

Figure 14 shows frequency spectra obtained on gauges 3 and 5. The fundamental and the harmonic waves are well represented by the models, but their amplitudes differ. The FLUINCO and the COULWAVE results are closer for the two gauges. There are some differences from those obtained by BOUSSiiW, especially on gauge 5, which does not show the presence of the fourth harmonic and the following.

Streamlines during one wave period obtained by FLUINCO are presented in Fig. 15. Unlike the previous case, a vortex, located between the upstream slope and the bottom, occurred during part of the wave period.

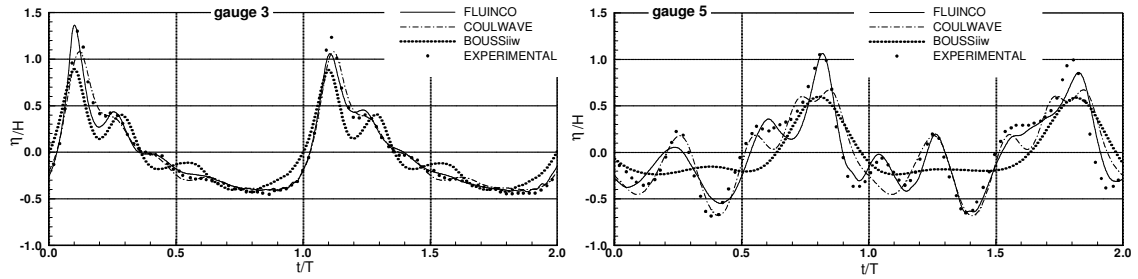

Figure 13: Free surface elevation for the 1:2 breakwater on gauges 3 and 5.

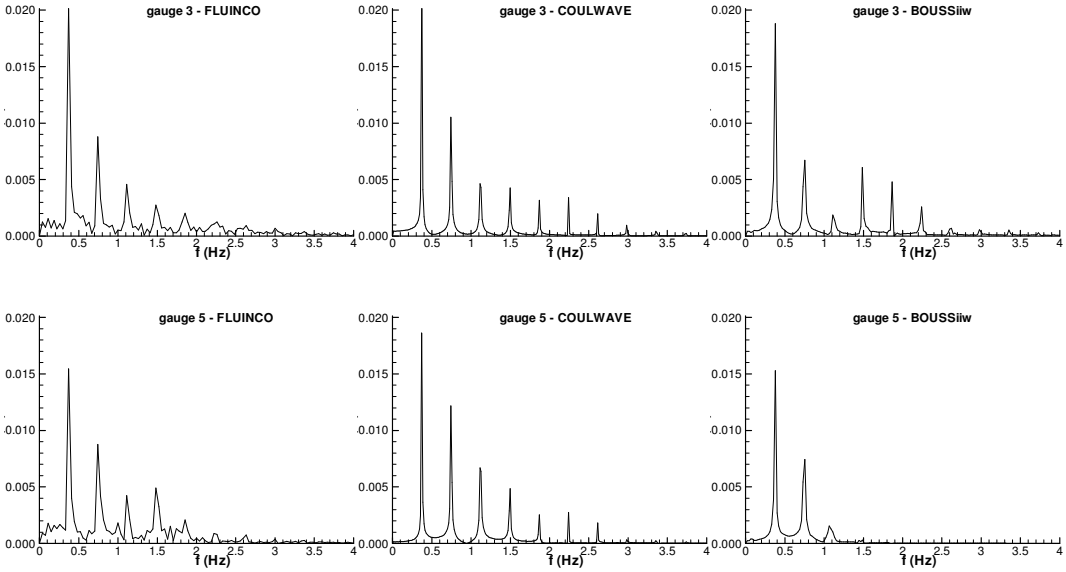

Figure 14: 1:2 Breakwater case. Frequency spectra on gauges 3 and 5.

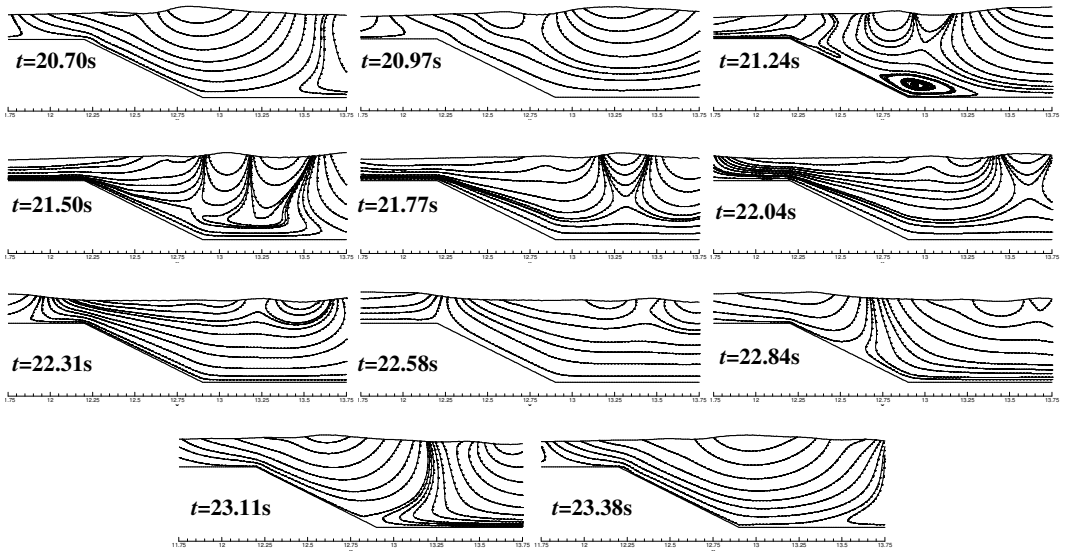

Figure 15: Streamlines of the 1:2 breakwater

3.3 Horizontal cylinder case

This case consists in a 5.2m long and 0.425m deep channel with a submerged cylinder of r = 0.025m positioned 1.60m from the wave generator (Fig. 16). The cylinder center is 0.075m (3r) from the free surface. The frequency wave is f=1.4 Hz; its amplitude is a = 0.0119 m and its wavelength is L=0.796 m, characterizing a deep water case.

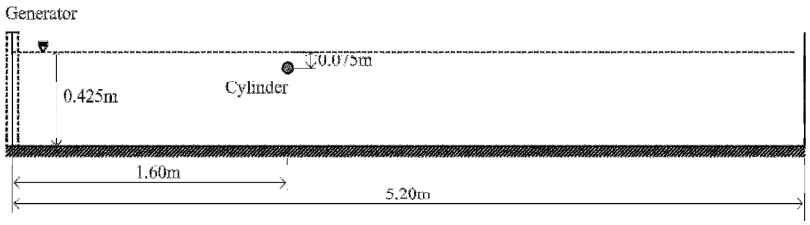

Figure 16: Geometry of the horizontal cylinder case.

Table 5 shows the period, the frequency and the wavelength for the fundamental frequency and its 2nd, 3rd and 4th harmonics, according to the linear wave theory.

	Fundamental	**2nd harmonic**	**3rd harmonic**	**4th harmonic**
Period, *T* (s)	0.7143	0.3571	0.2381	0.1786
Frequency, *f* (Hz)	1.4	2.8	4.2	5.6
Wavelength, *L*(m)	0.796	0.199	0.0885	0.0498

Table 5: Period, frequency and wavelength of the fundamental frequency and its 2nd, 3rd and 4th harmonics.

The mesh, with 173900 nodes and 515623 elements, has one layer of elements in the transversal direction. The average element size on the cylinder boundary is 0.0015 m (105 divisions in the circumference). The element size diminishes from the ends to the region near the cylinder and from the bottom to the free surface. The element sizes on the end where the wave generator is located and on the opposite end are 0.015 m (53 points per fundamental wavelength) and 0.02 m (40 points per fundamental wavelength), respectively. On the bottom, 0.0015m is also used.

The initial conditions are: null velocity components in all domain and hydrostatic pressure (null on the free surface). The wave is generated by imposing the surface elevation and the velocity components. The non-slip condition is imposed to the bottom and to the cylinder wall. The time step is 0.0002s, which satisfies the courant stabilized condition.

Figure 17 shows the free surface elevation obtained by the code and experimental tests, where *xc* is the horizontal coordinate of the cylinder center. In general, there is agreement between numerical and experimental results. We can notice the free surface disturbance downstream the cylinder. When (*x*-*xc*)/L is above 1.7, the numerical results are smoother than the experimental ones, showing the necessity of a refinement in this region.

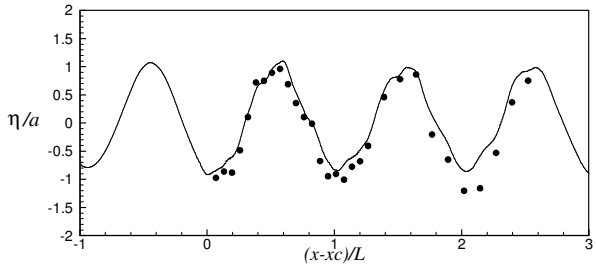

Figure 17: Horizontal cylinder case. Free surface elevation (Numerical — ; Experimental ■).

Figure 18 shows a comparison among numerical and experimental results in terms of free surface elevation on four gauges located at (*x*-*xc*)/L equal to -0.503, 0.0692, 0.509 and 1.264 (there is only a numerical result on the first gauge). We can observe the similarity among numerical and experimental results.

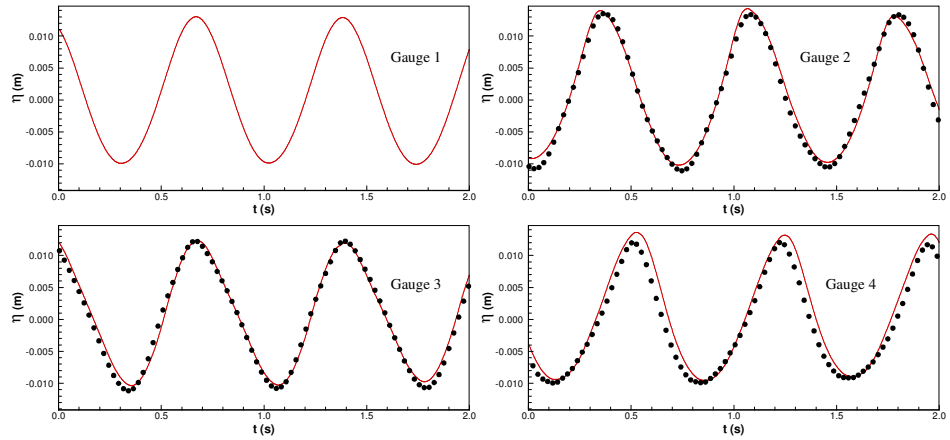

Figure 18: Free surface elevations on the gauges located at (*x*-*xc*)/*L* equal to -0.503, 0.0692, 0.509 and 1.264 (Numerical — ; Experimental ●).

Figure 19 shows the streamlines and the velocity modulus distribution at the same instant used in Figure 3. Recirculation and separation cannot be observed at downstream. Due to the oscillatory flow behavior, there is no time for recirculation productions. We can notice the flow acceleration near the cylinder due to the boundary layer effect. The viscous effects have only local influence, without modifying the velocity field far from it.

In Figures 20 and 21, velocity component profiles, u and v, on the same gauge positions are presented. These profiles were constructed at the same instant as those used in Figure 3. According to the linear theory, the maximum value for both horizontal and vertical components are equal to 0.105 m/s. For horizontal components, these values occur on the crest and the trough, while for vertical ones, these values occur on upward and downward zero-crossings. When one component is the maximum, another is null, because the phase difference is 90 degrees.

Gauge 1 ((*x*-*xc*)/L = -0.503) is located upstream, near the wave crest; no significant disturbance in u and v profiles is observed. The horizontal velocity component is positive and its maximum value is similar to the theoretical value in the crest. The wave trough passes by gauge 2; the vertical velocity component presents low values and the horizontal velocity component has negative values, reaching the maximum absolute value close to the theoretical ones (0.105 m/s). Gauge 3 is located near the first crest upstream, resulting in high horizontal component values. Finally, gauge 4 is on a region between the trough and upward zero-crossing. Both component profiles are negative and the vertical component magnitude shows how close the gauge is to upward zero-crossing.

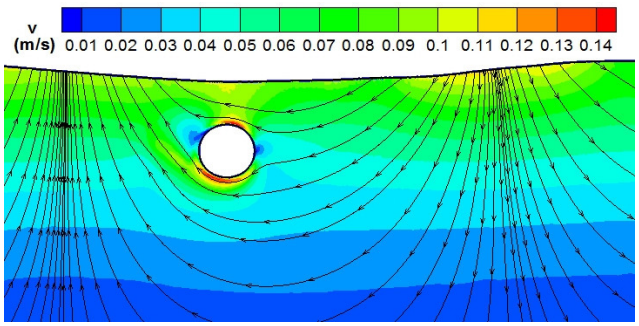

Figure 19: Streamlines and velocity modulus at the instant in which the free-surface elevation was captured (Fig. 17).

The non-slip boundary condition on the bottom does not change the general behavior of the wave propagation, because this case is considered a deep water one.

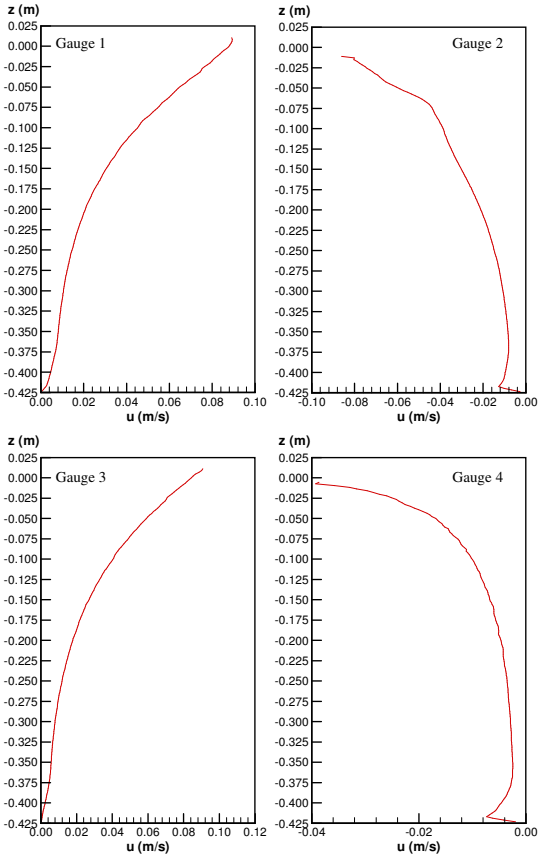

Figure 20: Horizontal velocity components at the same instant used in Figures 3 and 5 along the depth on gauges located at $(x\text{-}xc)/L$ equal to -0.503, 0.0692, 0.509 and 1.264.

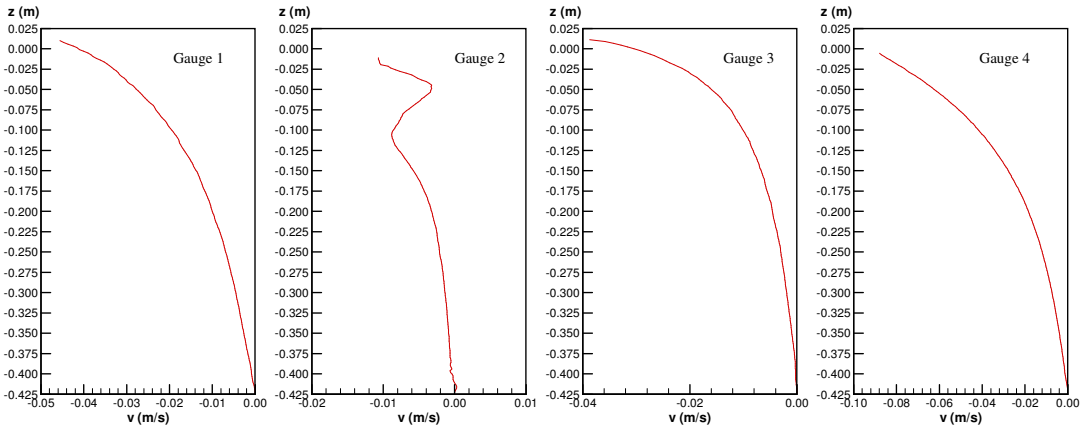

Figure 21: Vertical velocity components at the same instant used in Figures 3 and 5 along the depth on gauges located at $(x\text{-}xc)/L$ equal to -0.503, 0.0692, 0.509 and 1.264.

4 CONCLUSIONS

In this paper, three case studies related to wave propagation were analyzed numerically by applying the FLUINCO model. This model is based on the semi-implicit two-step Taylor Galerkin method to discretize the complete Navier-Stokes equations in time and space. A linear tetrahedral element and an ALE formulation to follow the free surface movements are adopted.

The model was initially applied to the wave propagation over a constant depth channel case. The free surface elevation and the velocity components along the time and the depth were compared with linear and non-linear theoretical ones, showing good similarity.

The second study case was concerned with the wave propagation over trapezoidal breakwaters. We analyzed two types of slopes: 1:20 and 1:10, and both 1:2. The results for the 1:20 and 1:10 breakwater slopes were compared with experimental ones developed by Dingemans (1994). The free surface elevations and the energy spectra on some gauges along the channel showed that the model presented good results. A little sub estimation of the maximum and minimum values indicates the necessity of a mesh refinement, mainly in zones where the non-linear phenomena increase. We have noticed that the flow separation does not occur, according to the streamline analyzes. In the second breakwater case (both slopes 1:2), the non-linearity increased. The free surface elevations and frequency spectra showed similarities between model and experimental (Ohyama, 1995) results. They were compared with Boussinesq model results and we could notice the superiority of a code that is based on the Navier-Stokes equations. In this case, the streamlines showed the presence of a vortex during a time interval in which erosion may happen in this region.

The third case was about the wave propagation over a submerged cylinder. The free surface elevations and velocity profiles obtained by FLUINCO were similar to experimental ones. The numerical results presented a smooth free surface deformation downstream, possibly because of the lack of refinement that caused numerical diffusion. In this case, the viscous effects influenced the flow behavior locally; far from the cylinder, the viscosity was not important.

The study cases presented in this paper showed the capacity of the FLUINCO model to simulate the wave action over submerged structures in two dimensions. Because the code is based on the complete Navier-Stokes equations, it has good results when viscosity effects are important, although its high computational cost restricts the application to problems with limited dimension domains. However, it can be minimized by using parallel computation, since the FLUINCO code is written in FORTRAN language employing parallel resources.

Some 3D cases are being studied as well as the fluid-structure interaction, where the structure has a rigid movement.

REFERENCES

Agnon, Y.; Madsen, P.A.; Schaffer, H., A new approach to high order Boussinesq models. *Journal of Fluid Mechanics*, 399: 319-333, 1999.

Bateman, W.J.D.; Swan, C.; Taylor, P.H., On the efficient numerical simulation of directionally spread surface water waves, *J. Comput. Phys*., 174(1):.277-305, 2001.

Beji, S., and Battjes, J.A., Experimental investigation of wave propagation over a bar, Coastal Engineering, 19: 151-162, 1993.

Beji, S., and Battjes, J.A., Numerical simulation of nonlinear wave propagation over a bar, Coastal Engineering, 23: 1-16, 1994.

Casulli, V., A semi-implicit finite difference method for non-hydrostatic, free-surface flows, Int. J. Numer. Meth. Fluids, 30: 425-440, 1999.

Casulli, V., and Stelling, G.S., Numerical simulation of 3D quasi-hydrostatic, free-surface flows, *J. Hydr. Eng. ASCE*, 124: 678-686, 1998.

Chakrabarti, S.K., Hydrodynamics of offshore structures, Computational Mechanics Publications, 1994.

Dean, R.J., and Dalrymple, R.A., Coastal processes with engineering applications, Cambridge University Press, 2002.

Dingemans, M.W., Comparation of computations with Boussinesq-like models and laboratory measurements, Report H-1684.12 Delft Hydraulics, 1994.

Dommermuth, D.G., and Yue, D.K.P., A high-order spectral method for the study of nonlinear gravity waves, *J. Fluid Mech*., 184: 267-288, 1987.

Flather, R.A., A tidal model of the northwest European continental shelf, *Mem. Soc. R. Liege*, 6 (10): 141-164, 1976.

Gobbi, M.F., and Kirby, J.T., Wave evolution over submerged sills: Tests of a high-order Boussinesq model. *Coastal Engineering*, 37: 57-96, 1999.

Grilli, S.T.; Guyenne, P.; Dias, F., A fully non-linear model for three-dimensional overturning waves over an arbitrary bottom, *Int. J. Numer. Meth. Fluids*, 35(7): 829-867, 2001.

Harlow, F.H., and Welch, J.E., Numerical calculation of time-dependent viscous incompressible flow, *Phys. Fluids*, 8: 2182-2189, 1965.

Hieu, P.D.; Katsutohi, T.; Ca, V.T., Numerical simulation of breaking waves using a two-phase flow model, *Appl. Math. Model*., 28: 983-1005, 2004.

Hodges, B.R., and Street, R.L., On simulation of turbulent nonlinear free-surface flows, *J. Comput. Phys*., 151: 425-457, 1999.

Huang, C.J., and Dong, C.M., Wave deformation and vortex generation in water waves propagating over a submerged dike, *Coastal Engineering*, 37: 123-148, 1999.

Huang, C.J. and Dong, C.M., On the interaction of a solitary wave and a submerged dike, *Coastal Engineering*, 43: 265-286, 2001.

Hsiao, S.C.; Lynett, P.; Hwung, H.H., Liu, P.L.F., Numerical simulations of nonlinear short waves using a multilayer model, *ASCE, J. Eng. Mech*., 131: 231-243, 2005.

Iafrati, A.; Di Mascio, A.; Campana, E.F., A level set technique applied to unsteady free surface flows, *Int. J. Numer. Meth. Fluids*, 35: 281-297, 2001.

Isaacson, M., Non-linear wave effects on fixed and floating bodies, *J. Fluid. Mech*., 120:.267-281, 1982.

Johnson, J.W.; Fuchs, R.A.; Morison, J.R., The damping action of submerged breakwaters, *Trans. Am. Geophys. Union*, 32: 704-718, 1951.

Jolas, P., Passage de la houle sur un seuil, *Houille Blanche*, 2: 148-152, 1960.

Kennedy, A.B.; Kirby, J.T.; Chen, Q.; Dalrymple, R.A., Boussinesq-type equations with improved nonlinear behaviour. *Wave Motion*, 33: 225-243, 2001.

Lin, P., and Li, C.W., A σ-coordinate three-dimensional numerical model for surface wave propagation, Int. J. Numer. Meth. Fluids, 38: 1045-1068, 2002.

Lin, P., and Liu, P.F.L., A numerical study of breaking waves in the surf zone, *J. Fluid Mech*., 359: 239-264, 1998.

Liu, P.L.F., Model equations for wave propagations from deep to shallow water. *Adv. Coast. Ocean Eng.*, 1:125-158, 1995.

Longuet-Higgins, M.S., and Cokelet, E.D., The deformation of steep surface waves on water. I. A numerical method of computation, *Proceedings of the Royal Society of London A,* 95: 1-26, 1976.

Lynett, P., and Liu, PL-F., A two-layer approach to water wave modelling. *Proceedings of the Royal Society of London A*, 460: 2637– 2669, 2004.

Madsen, P.A.; Murray, R.; Sorensen, O.R., A new form of Boussinesq equations with improved linear dispersion characteristics, *Coast Engrg*, 15: 371-388, 1991.

Madsen, P.A.; Bingham, H.B.; Liu, P.L.F., A new Boussinesq method for fully nonlinear waves from shallow to deep water, *J. Fluid Mech*., 462: 1-30, 2002.

Mahadevan, A.; Oliger, J.; Street, R., A non-hydrostatic mesoscale ocean model. Part 1: Well-posedness and scaling, *J. Phys. Oceanogr*., 26: 1868-1880, 1996.

Marshall, J.; Adcroft, A.; Hill, C.; Perelman, L.; Heisey, C., A finite-volume, incompressible Navier-Stokes model for studies of the ocean on parallel computers, *J. Geophys. Res*., 102: 5753-5766, 1997.

Nwogu, O., An alternative form of Boussinesq equations for nearshore wave propagation. *J. Waterway, Port, Coastal Engineering*, 119: 618-638, 1993.

Ohyama, T.; Kioka, W.; Tada, A., Applicability of numerical models to nonlinear dispersive waves, *Coastal Engineering*, 24: 297-313, 1995.

Peregrine, D.H., Long waves on a beach, *J. Fluid Mech*., 27: 815-882, 1967.

Pinheiro. L., Um método de elementos finitos para a discretização das equações de Boussinesq estendidas. Tese de mestrado. Engenharia Mecânica, IST, 2007.

Ramaswamy, R., and Kawahara, M., Arbitrary lagrangian-eulerian finite element method for unsteady, convective, incompressible viscous free surface fluid flow, *International Journal for Numerical Methods in Fluids*, 7: 1053-1075, 1987.

Schäffer, H.A, and Madsen, P.A., Further enhencements of Boussinesq-type equations. *Coastal Engineering*, 26: 1-14, 1995.

Shen, Y.M.; Ng, C.O.; Zheng, Y.H., Simulation of wave propagation over a submerged bar using the VOF method with a two-equation k-epsilon turbulence modeling, *Ocean Engineering*, 31: 87-95, 2004.

Stansby, P.K., and Zhou, J.G., Shallow-water flow solver with non-hydrostatic pressure: 2D vertical plane problems, *Int. J. Numer. Meth. Fluids*, 28: 514-563, 1998.

Stelling, G.S., and Zijlema, M., Further experience in computing non-hydrostatic free-surface flow involving with water waves, *Int. J. Numer. Meth. Fluids*, 48: 169-197, 2005.

Teixeira, P.R.F., and Awruch, A.M., Numerical simulation of three dimensional incompressible flows using the finite element method, *ENCIT*, n.8, Porto Alegre, 2000.

Teixeira, P.R.F., and Awruch, A.M., Numerical simulation of fluid-structure interaction using the finite element method, *Computers Fluids*, 34: 249-273, 2005.

Ting, F.C.K., and Kim, Y.K., Vortex generation in water-waves propagating over a submerged obstacle, *Coastal Engineering*, 24: 23-49, 1994.

Wei, G.; Kirby, J.T.; Grilli, S.T.; Subramanya, R., A fully nonlinear Boussinesq model for surface waves. Part 1. Highly nonlinear unsteady Wave, *J. Fluid Mech.,* 294: 71-92, 1995.

Wu, T.Y., A unified theory for modelling water waves. *Advances Mechanics*, 37:1-88, 2001.

Yuan, H.L., and Wu, C.H., A two-dimensional vertical non-hydrostatic σ model with an implicit method for free-surface flows, *Int. J. Numer. Meth. Fluids*, 44: 811-835, 2004.

Zijlema, M., and Stelling, G.S., Efficient computation of surf zone waves using the nonlinear shallow water equations with non-hydrostatic pressure, *Coastal Engineering*, 55: 780-790, 2008.

Zhou, J.G., and Stansby, P.K., An arbitrary Lagrangian-Eulerian σ (ALES) model with non-hydrostatic pressure for shallow water flows, *Comput. Meth. Appl. Mech. Eng*., 178: 199-214, 1999.